Combining organic cations of different sizes grants improved control over perovskitoid dimensionality and bandgap

Isaiah Gilley, Hyoung Woo Kwon, Cheng Liu, Yi Yang, Chuying Huang, Haoyue Wan, Abdulaziz Bati, Evan Oriel, Mikaël Kepenekian, Badri Vishal, et al.

Combining organic cations of different sizes grants improved control over perovskitoid dimensionality and bandgap

Isaiah W. Gilley,[1] Hyoung Woo Kwon,[1] Cheng Liu,[1] Yi Yang,[1] Chuying Huang,[1] Haoyue Wan,[1] Abdulaziz S. R. Bati,[1] Evan H. Oriel,[1] Mikaël Kepenekian,[2] Badri Vishal,[3] Stefan Zeiske,[1] Khasim Saheb Bayikadi,[1] Taylor E. Wiggins,[1] Eugenia S. Vasileiadou,[1] Bin Chen,[1,4] Richard D. Schaller,[1,5] Jacky Even,[4] Stefaan De Wolf,[3] Edward H. Sargent,[1,6] Mercouri G. Kanatzidis[1*]*

[1]Department of Chemistry, Northwestern University, 2145 Sheridan Rd, Evanston, IL 60208, United States

[2]Univ Rennes, ENSCR, INSA Rennes, CNRS, ISCR (Institut des Sciences Chimiques de Rennes), UMR 6226, Rennes F-35000, France

[3]Center for Renewable Energy and Storage Technologies (CREST), Physical Sciences and Engineering Division (PSE), King Abdullah University of Science and Technology (KAUST), Thuwal 23955-6900, Kingdom of Saudi Arabia

[4]Univ Rennes, INSA Rennes, CNRS, Institut FOTON, UMR 6082, Rennes F-35000, France

[5]Center for Nanoscale Materials, Argonne National Laboratory, Lemont, IL 60439, USA

[6]Department of Electrical and Computer Engineering, Northwestern University, 2145 Sheridan Rd, Evanston, IL 60208, United States

[*]Corresponding Authors: ted.sargent@northwestern.edu, m-kanatzidis@northwestern.edu

ABSTRACT

Because mixed-halide wide-bandgap (1.6-2.0 eV) perovskite solar cells suffer from operating instability related to light-induced halide segregation, it is of interest to study alternative means of bandgap widening. Perovskitoids combine wide bandgaps and structural stability resulting from face- or edge-sharing octahedral connections in their crystal structures. Unfortunately, there existed no prior reports of three-dimensional (3D) perovskitoids having direct bandgaps with optical absorption edges less than 2.2 eV. As the most significant predictor of perovskitoid bandgaps is the fraction of corner-sharing in their crystal structures, we hypothesized that increasing the amount of corner-sharing would access lower bandgaps than previously reported. We accomplished this by mixing a spacer cation within the size range for 3D perovskitoid formation with a smaller, perovskite-forming cation. We explored three spacer cations of different sizes: ethylammonium (EA), cyclopropylammonium (c-C3A), and cyclobutylammonium (c-C4A), combining these with methylammonium (MA), and found that the middle cation, c-C3A, pairs with MA to form a 3D perovskitoid with the formula $(c\text{-}C3A)_3(MA)_3Pb_5I_{16}$ and a direct bandgap with an optical absorption edge at 2.0 eV. Solution-processed films of this perovskitoid showed improved light stability over mixed-halide perovskites, and solar cells based on these films exhibit increased maximum power point operating stability compared to reference mixed-halide devices.

INTRODUCTION

Perovskite solar cells have seen rapid progress in power conversion efficiency and feature solution processing and earth-abundant compositions.[1] Multi-junction perovskite solar cells can, in principle, achieve higher theoretical maximum efficiencies[2] than single-junction devices by reducing thermalization losses. However, to date, perovskite compositions with bandgaps above 1.6 eV have been limited in their operating stability by light-induced halide segregation.[3]

To address halide segregation, molecular additives have been employed to inhibit halide ion migration,[4-7] but these additives have also curtailed charge transport.[8] Two-dimensional (2D) perovskites have bandgaps widened via dimensional reduction[9] and do feature enhanced light stability compared to 3D counterparts.[10, 11] However, their higher exciton binding energies, anisotropic charge transport, and spontaneous phase disproportionation during processing have limited their employment as absorbing layers.[11-14]

While perovskites consist solely of corner-shared octahedra, the wider family of perovskitoids feature octahedral face- or edge-sharing in addition to corner-sharing in their crystal structures.[15-20] This altered octahedral connectivity affords perovskitoids wider bandgaps than perovskites without the need for halide mixing or dimensional reduction. The bandgaps of reported perovskitoids are strongly correlated with the connectivity of the structures, with highly corner-sharing perovskitoids having the narrowest bandgaps.[21-30] Perovskitoids have been recently reported as photodetectors,[31] X-ray and γ-ray detectors,[18, 23] and passivating layers for perovskite solar cells.[15, 32]

We hypothesized that a 3D single-halide (all-iodide) perovskitoid with sufficient corner-sharing could achieve an optical absorption edge of interest for triple-junction solar cells (1.7-2.0 eV). This would require us to synthesize narrower bandgap perovskitoids than have yet been documented, for the narrowest absorption edge among direct bandgap 3D lead iodide perovskitoids reported to date is 2.2 eV.[21-30] Designing a perovskitoid with a desired bandgap and dimensionality is challenging because the diverse connectivity of perovskitoids complicates the prediction of their crystal structures and optoelectronic properties. We began, therefore, by seeking design principles for 3D perovskitoids, where the size, shape, and stoichiometry of organic cations are key determinants of the structure and properties.

RESULTS AND DISCUSSION

Small organic cations favor a 3D perovskite structure, while large ones break up the structure, reducing dimensionality. Thus, the formation of 3D perovskitoids should follow a Goldilocks principle for cations capable of expanding the structure without altering its dimensionality (Figure 1a). A survey of published 3D lead halide perovskitoids suggests that these structures tend to be templated by organic cations with effective diameters of 3-6 Å, but some outliers contain cations up to 12 Å.[21-30, 33-55] However, these outliers are typically less connected and have wider bandgaps than those with small cations, so the 3-6 Å range appears optimal for the formation of perovskitoids with photovoltaic-relevant absorption. To access a higher fraction of corner-sharing than previously reported ternary perovskitoids, a cation falling within this size range should be mixed with a perovskite-forming cation such as cesium, methylammonium, or formamidinium to bring the structure of the perovskitoid closer to the 3D perovskite structure. We selected cyclopropylammonium (c-C3A) for this study because it falls within this size range, and the corresponding quaternary phase with methylammonium (MA) is not reported.

Despite falling within the 3-6 Å size range for 3D perovskitoid formation, c-C3A forms a ternary 2D perovskite, $(c\text{-}C3A)_2PbI_4$, in combination with PbI_2.[56] However, we found that when MA is included in the reaction mixture, c-C3A templates a novel 3D perovskitoid with the formula $(c\text{-}C3A)_3(MA)_3Pb_5I_{16}$. Thus, the addition of MA 'unlocks' the 3D perovskitoid phase of c-C3A. Furthermore, the fraction of corner-sharing in this perovskitoid is 69%, higher than any other reported lead iodide perovskitoid (Figure 1b).[21-30] Because MA can fit into small pockets within the crystal structure, it accesses higher fractions of corner-sharing than have been seen in ternary compositions. In this case, MA serves as a 'perovskitizer,' increasing the corner-sharing from 50% in $(c\text{-}C3A)_2PbI_4$ to 69% in $(c\text{-}C3A)_3(MA)_3Pb_5I_{16}$, closer to the 100% corner-sharing of $MAPbI_3$. It is worth noting that allylamine and propylamine, other three-carbon amines, produce step-like 2D perovskitoids and, in MA rich stoichiometries, layered perovskites.[57, 58] As the ring shape of cyclopropylamine makes it slightly shorter than these chain molecules, the slight difference in size and shape of the cation results in a dramatic change in the crystal structure of the resulting quaternary phase.

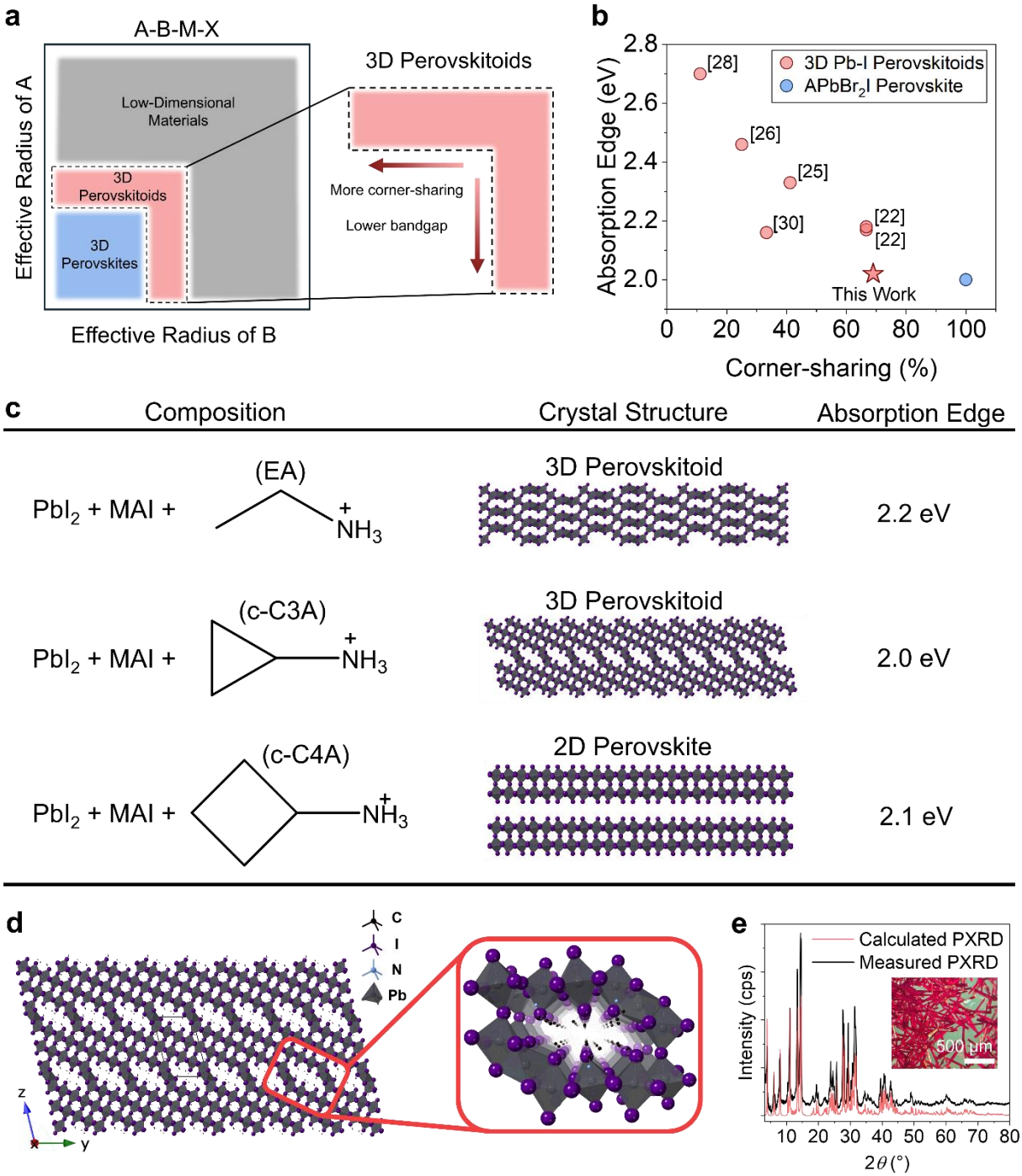

Figure 1. Effects of organic cation mixing and size control on perovskitoid structures. (a) Schematic representation of perovskitoid formation with respect to cation size for quaternary halometalates (A, B = organic cations; M = Sn Pb; X = Cl, Br, I). (b) Optical absorption edge vs. corner-sharing fraction for reported 3D lead iodide perovskitoids. (c) Comparison of the crystal structures and absorption edges for hybrid iodoplumbates synthesized with methylammonium (MA) and ethylammonium (EA), cyclopropylammonium (c-C3A), or cyclobutylammonium (c-C4A). (d) Crystal structure of (c-C3A)$_3$(MA)$_3$Pb$_5$I$_{16}$ shown down the *a*-axis with C, N, I, and Pb shown in black, blue, purple, and gray, respectively. (e) Calculated (red) and measured (black) powder X-ray diffraction patterns for red-colored (c-C3A)$_3$(MA)$_3$Pb$_5$I$_{16}$ with inset image of (c-C3A)$_3$(MA)$_3$Pb$_5$I$_{16}$ single crystals.

After finding that c-C3A forms a 3D perovskitoid with MA and PbI_2, we tested the generalizability of this observation by synthesizing analogous iodoplumbates based on EA and c-C4A, which are one carbon smaller and larger than c-C3A, respectively (Figure 1c). We chose EA and c-C4A to test whether incrementing or decrementing the size of the organic cation incorporated into the quaternary phase would significantly impact the resulting crystal structure. The smallest cation of the three, EA, forms a different 3D perovskitoid with a formula of $(EA)(MA)Pb_2I_6$, while the slightly larger c-C4A forms a 2D perovskite with a formula of $(c\text{-}C4A)_2(MA)Pb_2I_7$. Although EA and c-C3A both form 3D perovskitoids with MA, the c-C3A perovskitoid has significantly more corner-sharing in its crystal structure, with 69% corner-sharing as opposed to 50% in the EA perovskitoid. This higher fraction of corner-sharing is reflected in the absorption of the perovskitoids; $(EA)(MA)Pb_2I_6$ has an optical absorption edge of 2.2 eV while $(c\text{-}C3A)_3(MA)_3Pb_5I_{16}$ has an absorption edge of 2.0 eV, and $(c\text{-}C4A)_2(MA)Pb_2I_7$ has an absorption edge of 2.1 eV. As the ternary iodoplumbate based on EA is an all-face-sharing structure,[59] the formation of a 50% face-sharing 3D perovskitoid in $(EA)(MA)Pb_2I_6$ suggests that the EA cation is too small to stabilize a 3D perovskitoid with a sufficient fraction of corner-sharing for photovoltaic-relevant absorption. Likewise, the formation of a 2D perovskite in $(c\text{-}C4A)_2(MA)Pb_2I_7$ suggests that c-C4A is too large to template a 3D perovskitoid, instead preferring to adopt a lower dimensional, layered structure. However, c-C3A appears to exist within a narrow sweet spot for 3D perovskitoid formation as $(c\text{-}C3A)_3(MA)_3Pb_5I_{16}$ retains 3D connectivity while achieving an absorption edge ideal for all-perovskite triple-junction solar cells. More detailed structure images and electronic absorption spectra for $(EA)(MA)Pb_2I_6$ and $(c\text{-}C4A)_2(MA)Pb_2I_7$ are provided in the Supporting Information (Figures S1-S3).

$(c\text{-}C3A)_3(MA)_3Pb_5I_{16}$ crystallizes in the triclinic space group $P\bar{1}$ with unit cell parameters a = 8.8784(2) Å, b = 15.5291(4) Å, c = 23.1301(7) Å, α = 103.159(2)°, β = 91.397(2)°, and γ = 106.169(2)°. The crystal structure (Figure 1d) is comprised of three-octahedra thick $[Pb_4I_{16}]^{8-}$ slabs taken from the ⟨311⟩ plane of the 3D perovskite crystal structure linked together by face-sharing octahedra, which completes the 3D $[Pb_5I_{16}]^{6-}$ inorganic lattice. The MA cation sits in the small space between the corner-sharing PbI_6 octahedra, while the c-C3A cation sits in the 'tunnels' created by the face-sharing octahedra, breaking up the otherwise layered structure (Figure 1d). This structure resembles the 'step-like' layered perovskitoids previously reported with allylammonium[58] and propylammonium,[57, 60] but the tighter packing of $(c\text{-}C3A)_3(MA)_3Pb_5I_{16}$

forces the perovskitoid layers together, generating 3D connectivity. The (c-C3A)$_3$(MA)$_3$Pb$_5$I$_{16}$ perovskitoid contains both face-sharing and corner-sharing octahedra, and the fraction of corner-sharing in the structure is 68.75%. This high fraction of corner-sharing should lend the compound a narrower bandgap and better charge-transport properties than other 3D lead iodide perovskitoids. Powder X-ray diffraction (PXRD) patterns show that the bulk phase produced during synthesis matches the reported single crystal structure (Figure 1e). Notably, single-crystal syntheses of (c-C3A)$_3$(MA)$_3$Pb$_5$I$_{16}$ often produce a mixture of the desired perovskitoid with an impurity non-perovskite hydrate phase, (c-C3A)$_x$(MA)$_{1-x}$PbI$_3$•H$_2$O. This hydrate is minimized during single crystal synthesis by extracting the crystals from their mother liquor before a significant amount of hydration occurs. More information about this hydrate and its crystal structure are provided in the Supporting Information (Figures S4-S6).

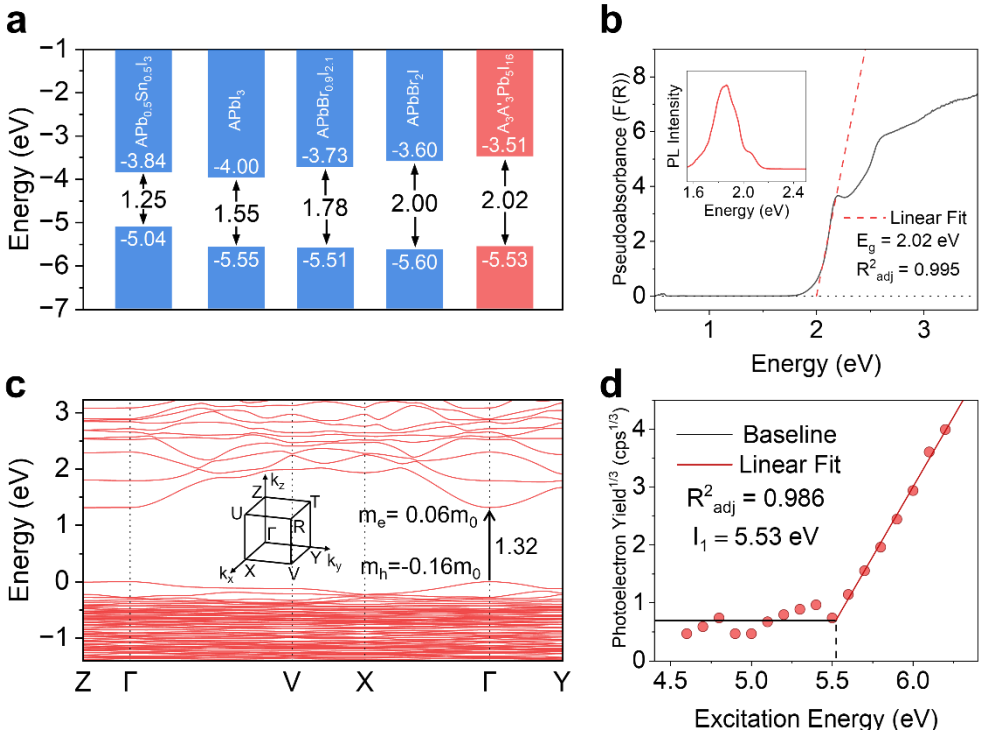

Figure 2. Optical and electronic properties of (c-C3A)$_3$(MA)$_3$Pb$_5$I$_{16}$. (a) Band alignment of (c-C3A)$_3$(MA)$_3$Pb$_5$I$_{16}$ (red) alongside 3D perovskites (blue) with 1.25, 1.55, 1.78, and 2.00 eV bandgaps. (b) Diffuse-reflectance spectrum of (c-C3A)$_3$(MA)$_3$Pb$_5$I$_{16}$ with optical absorption edge fit to 2.02 eV and inset photoluminescence spectrum of (c-C3A)$_3$(MA)$_3$Pb$_5$I$_{16}$ thin film. (c) Band-structure of (c-C3A)$_3$(MA)$_3$Pb$_5$I$_{16}$. (d) Photoelectron yield spectroscopy in air spectrum of (c-C3A)$_3$(MA)$_3$Pb$_5$I$_{16}$ with first ionization energy fit to 5.53 eV.

The band alignment of $(c\text{-}C3A)_3(MA)_3Pb_5I_{16}$ was investigated by a combination of diffuse reflectance UV-vis spectroscopy and photoemission yield spectroscopy in air to determine the absorption edge and absolute energy of the valence band maximum, respectively (Figure 2a). Diffuse reflectance spectroscopy (Figure 2b) confirms the optical absorption edge is 2.02 eV, within the ideal range of for a wide-bandgap top-cell in triple- or quadruple-junction solar cells,[2] and band structure calculations confirm the direct nature of the bandgap (Figure 2c). Notably, $(c\text{-}C3A)_3(MA)_3Pb_5I_{16}$ has the narrowest optical absorption edge reported for any direct bandgap Pb perovskitoid phase.[21-30] Photoemission yield spectroscopy in air (Figure 2d) yields a valence band maximum of -5.53 eV, very close to the experimentally determined valence band maxima for the 1.55, 1.78, and 2.00 eV bandgap 3D perovskites, respectively (Figure S7). The conduction band, determined by adding the optically determined bandgap to the valence band energy, is -3.51 eV for $(c\text{-}C3A)_3(MA)_3Pb_5I_{16}$, in close alignment with the conduction band of the 2.00 eV 3D perovskite at -3.60 eV.

Photoluminescence (PL) spectra were measured on $(c\text{-}C3A)_3(MA)_3Pb_5I_{16}$ films (Figure 2b, inset). The film PL shows two distinct features. A small shoulder peak centered around 610 nm likely corresponds to direct band-to-band relaxation within the perovskitoid, but a larger peak around 650 nm produces an overall broad luminescence spectrum with a full-width at half-maximum of 80 nm and an average Stokes shift of 40 nm. Low-frequency Raman spectroscopy on the same films at room temperature reveals a centralized, broad peak (Figure S8) similar to that of $MAPbBr_3$ and $CsPbBr_3$,[61, 62] indicating that $(c\text{-}C3A)_3(MA)_3Pb_5I_{16}$ experiences dynamic structural disorder analogous to that of 3D perovskites. A photodetector fabricated from a single crystal of $(c\text{-}C3A)_3(MA)_3Pb_5I_{16}$ a more than 20x increase in current when exposed to room lighting, suggesting a high degree of photoresponsivity (Figure S9). The full PL spectrum of powder and films of $(c\text{-}C3A)_3(MA)_3Pb_5I_{16}$ along with details on $(c\text{-}C3A)_3(MA)_3Pb_5I_{16}$ films, including photographs, scanning electron micrographs, transmission electron micrographs, transient absorbance, and XRD are provided in the Supporting Information (Figures S10-S13).

The electronic band-structure of $(c\text{-}C3A)_3(MA)_3Pb_5I_{16}$ (Figure 2c) shows a direct bandgap at Γ with band edges comprised of hybridized lead and iodide orbitals, consistent with reported lead halide perovskites (Figure S14).[63] This leads to high dispersion, particularly in directions where octahedra are corner-shared. However, the region from Γ to *Z* presents nearly flat bands

with bandwidths smaller than 5 meV, corresponding to the real direction of the face-sharing connections between corner-sharing layers of the crystal structure. This could suggest poor charge-transport between corner-sharing layers of the 3D perovskitoid, resulting in potentially anisotropic conductivity. Nevertheless, the high dispersion perpendicular to the face-sharing direction indicates generally good charge-transport within $(c\text{-}C3A)_3(MA)_3Pb_5I_{16}$. The effective masses of electrons (m_e) and holes (m_h) at the band edges in the 3D perovskitoid are 0.06 and -0.16 times the mass of an electron (m_0), respectively. The m_h in the perovskitoid is similar in magnitude to the computed m_h in $CsPbI_3$ of $-0.11m_0$,[64, 65] while m_e of the perovskitoid is lower than m_e in $CsPbI_3$ of $0.10m_0$.[64, 65] It should be noted that the effective masses for the perovskitoid are calculated at the band minima and in the direction of corner-sharing Pb-I-Pb bonds, and the effective masses in other directions, particularly in the direction of face-sharing, are likely higher. The relatively narrow bandgap and 3D crystal structure of $(c\text{-}C3A)_3(MA)_3Pb_5I_{16}$ make the phase uniquely suited for demonstration of the first perovskitoid solar cells, and the low effective masses of electrons and holes in the perovskitoid, comparable to 3D perovskites, indicate that $(c\text{-}C3A)_3(MA)_3Pb_5I_{16}$ should be capable of sufficient charge-transport for solar cell applications. Furthermore, because the offset between the band alignments of the 2.00 eV mixed-halide perovskite and the 2.02 eV perovskitoid are relatively minor, it should be possible to assess the viability of $(c\text{-}C3A)_3(MA)_3Pb_5I_{16}$ by simply replacing the active layer in an existing architecture used for 2.00 eV 3D perovskite devices with the 3D perovskitoid.

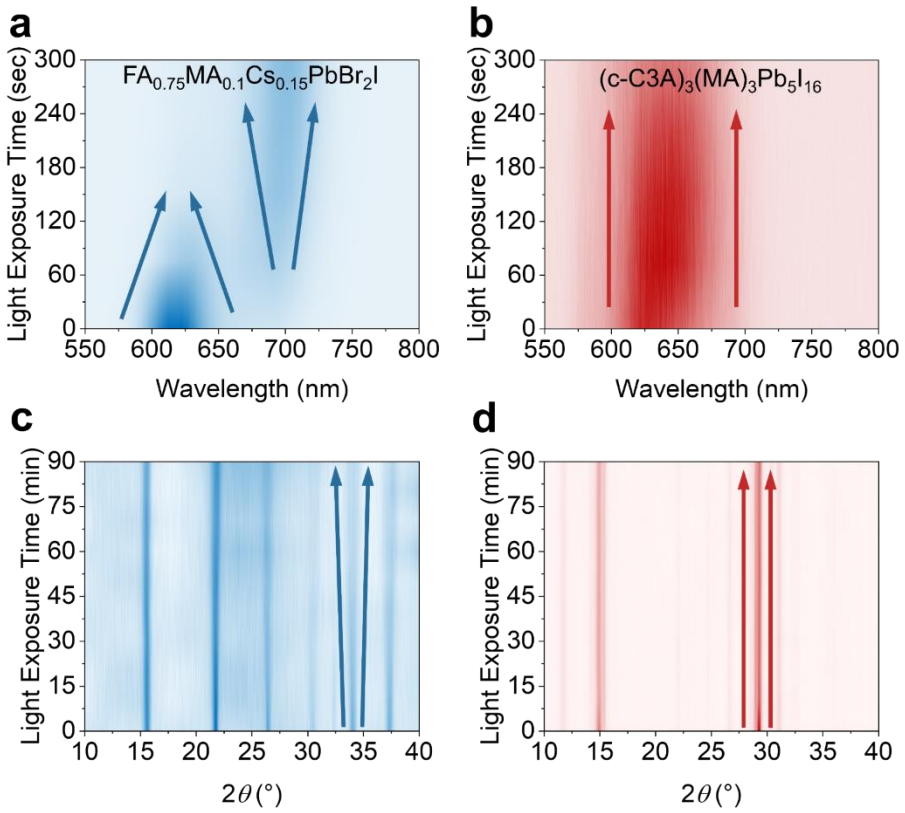

Figure 3. Light stability of 2.0 eV mixed-halide perovskite and $(c\text{-}C3A)_3(MA)_3Pb_5I_{16}$. (a) and (b) photoluminescence spectra for $(c\text{-}C3A)_3(MA)_3Pb_5I_{16}$ and 2.0 eV mixed-halide 3D perovskite films under continuous light exposure over 300 seconds with high intensity mapped as dark color and low intensity mapped as light color. (c) and (d) X-ray diffraction patterns of $(c\text{-}C3A)_3(MA)_3Pb_5I_{16}$ and 2.0 eV 3D perovskite films under continuous light exposure over 90 min.

We investigated the light stability of $(c\text{-}C3A)_3(MA)_3Pb_5I_{16}$ films by conducting PL and XRD measurements under continuous illumination and comparing the results to identical experiments performed on 2.0 eV mixed-halide perovskite films. The PL stability data for the mixed-halide perovskite (Figure 3a) was measured using confocal laser illumination and plotted as a function of time, under which the 2.0 eV PL peak shifts significantly after only 60 seconds, evidence of light-induced halide segregation. The $(c\text{-}C3A)_3(MA)_3Pb_5I_{16}$ film (Figure 3b), however, shows no significant peak shift over the same period. XRD stability (Figures 3c and 3d) was measured using global 1 sun white-light illumination, under which the 2.0 eV perovskite film diffraction peaks broaden and lose intensity over 90 minutes while the $(c\text{-}C3A)_3(MA)_3Pb_5I_{16}$ film diffraction peaks show no significant change, indicating that the perovskitoid film is phase-stable under 1 sun illumination. These results confirm that the elimination of halide-mixing from the composition of $(c\text{-}C3A)_3(MA)_3Pb_5I_{16}$ dramatically improves upon the light-stability of the 2.0 eV

mixed-halide perovskite. Thermal stability of bulk $(c\text{-}C3A)_3(MA)_3Pb_5I_{16}$ crystals and films is presented in the Supporting Information (Figures S15 and S16)

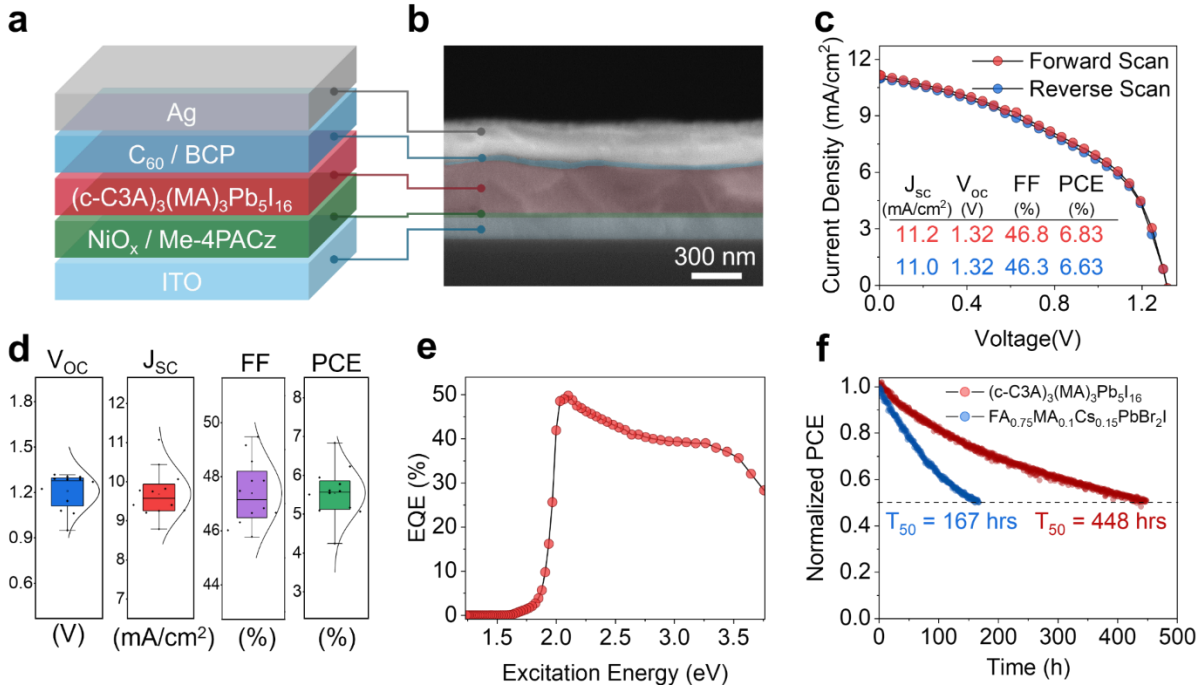

Figure 4. Solar cells of $(c\text{-}C3A)_3(MA)_3Pb_5I_{16}$. (a) Schematic diagram of $(c\text{-}C3A)_3(MA)_3Pb_5I_{16}$ single-junction solar cell architecture. (b) Cross-sectional SEM image of $(c\text{-}C3A)_3(MA)_3Pb_5I_{16}$ solar cell. (c) Current-voltage curve with device characteristics for champion $(c\text{-}C3A)_3(MA)_3Pb_5I_{16}$ solar cell including open-circuit voltage (V_{oc}), short-circuit current density (J_{sc}), fill-factor (FF), and power-conversion efficiency (PCE). (d) Device statistics for thirteen $(c\text{-}C3A)_3(MA)_3Pb_5I_{16}$ solar cells. (e) External-quantum yield spectrum of a $(c\text{-}C3A)_3(MA)_3Pb_5I_{16}$ solar cell. (f) Maximum power point tracking of $(c\text{-}C3A)_3(MA)_3Pb_5I_{16}$ and 2.0 eV 3D perovskite solar cells over 500 hours in N_2-filled glovebox. Data is cut to the time at which half of the initial efficiency is lost (T_{50}).

Solar cells of $(c\text{-}C3A)_3(MA)_3Pb_5I_{16}$ were fabricated with an architecture of ITO/NiO_x/Me-4PACz/3D perovskitoid/C_{60}/BCP/Ag (Figure 4a). Cross-sectional SEM images of the devices show a perovskitoid layer with a thickness of approximately 350 nm (Figure 4b). The current-voltage curve of the champion perovskitoid device (Figure 4c) has a remarkably high V_{oc} of 1.32 V. However, the efficiency of the perovskitoid device is limited by its short-circuit current density (J_{sc}) of 11.1 mA/cm^2 and fill-factor (FF) of 46.8% as compared to 12.8 mA/cm^2 and 83.0% for the record 2.0 eV 3D perovskite device.[66] These characteristics result in a PCE of 6.83% for the champion $(c\text{-}C3A)_3(MA)_3Pb_5I_{16}$ device, compared to 15.3% for the record 2.0 eV 3D perovskite.[66] Statistics for thirteen $(c\text{-}C3A)_3(MA)_3Pb_5I_{16}$ devices are provided in Figure 4d. The PCE difference between the perovskitoid and mixed-halide perovskite devices most likely arises from the quality of the perovskitoid film, which is also reflected in the external quantum efficiency (EQE) of the

perovskitoid devices (Figure 4e). Additionally, PXRD patterns of perovskitoid films indicate that they are strongly oriented preferential to the (001) plane of $(c\text{-}C3A)_3(MA)_3Pb_5I_{16}$ (Figure S11d), suggesting that charges are extracted from the film perpendicular to the corner-sharing layers of the perovskitoid. Furthemore, the diffuse reflectance spectrum of $(c\text{-}C3A)_3(MA)_3Pb_5I_{16}$ shows a minor feature characteristic of excitonic absorption. Should the exciton binding energy significantly exceed the ambient thermal energy, exciton formation could also inhibit the devices' J_{sc}. Likely, the charge-extraction and therefore J_{sc} and FF would be improved with a more favorable orientation of the perovskitoid film, such as a (010) or (100) 'vertical' orientation. Nevertheless, the $(c\text{-}C3A)_3(MA)_3Pb_5I_{16}$ devices were, as a first try, able to achieve more than half the record efficiency of the corresponding 3D perovskites, a promising initial result. Furthermore, the high V_{oc} of the perovskitoid devices is encouraging for future perovskitoid solar cell performance, and the low J_{sc} and FF may be ameliorated with improvements to film quality, film orientation, or device architecture. Light intensity-dependent JV, V_{oc}, and J_{sc} measurements along with photocurrent transients and photo-charge extraction by linearly increasing voltage (photo-CELIV) measurements are provided in the Supporting Information (Figures S17-19). A detailed analysis of these experiments is presented in the Supporting Information, but they suggest that the carrier mobility and charge transport properties of $(c\text{-}C3A)_3(MA)_3Pb_5I_{16}$ are similar to those of mixed-halide perovskites at the same bandgap, indicating that the perovskitoid devices are limited primarily by their low shunt resistance and high series resistance.

To investigate device stability under continuous illumination, we performed maximum power point tracking measurements under continuous one-sun illumination (Figure 4f). The $(c\text{-}C3A)_3(MA)_3Pb_5I_{16}$ devices demonstrate operating stability with T_{50} (the duration for the device efficiency to decay to 50% of the initial value) of 448 hours, 2.7 times longer than the 167-hour T_{50} of the 2.0 eV perovskite device, again confirming that the elimination of halide-mixing lends $(c\text{-}C3A)_3(MA)_3Pb_5I_{16}$ dramatically improved stability over 2.0 eV mixed-halide perovskites.

CONCLUSIONS

By leveraging cation size and ratio to control structural connectivity, we synthesized a 3D lead iodide perovskitoid with the lowest optical absorption edge reported to date, bringing the perovskitoid within the ideal range for triple-junction solar cells. To demonstrate the utility of these materials, we fabricated perovskitoid solar cells, which have an operating decay time 2.7x longer than cells based on mixed-halide perovskites at the same bandgap. The efficiency of these devices is limited in fill factor by the perovskitoid film morphology and orientation, resulting from constrained charge-transport in the direction of face-sharing connections within the perovskitoid crystal structure. To advance the efficiency of perovskitoid solar cells to levels comparable with perovskites, future research must focus on controlling crystallite growth during film formation and on designing new perovskitoid materials that enable more isotropic charge transport. We believe that an edge-sharing 3D perovskitoid could achieve these criteria, so future synthetic work should focus on controlling the type of sharing present within the perovskitoid. Nevertheless, such an edge-sharing perovskitoid would need to maintain a bandgap similar to or narrower than the perovskitoid presented in this work, so the bandgap control strategies presented herein will be critical in the development of perovskitoids as functional materials. Overall, we believe this report establishes perovskitoids as a notable and underrepresented class of materials for optoelectronics applications with exceptional structural diversity.

EXPERIMENTAL AND COMPUTATIONAL METHODS

Materials. All materials were used as received without further purification. Lead oxide (Alfa Aesar, 99.9%), cyclopropylamine (Oakwood Chemical), cyclobutylamine (Thermo Scientific, 98%), methylamine hydrochloride (Aldrich, ≥98%), ethylamine hydrochloride (Aldrich, 98%), hypophosphorous acid (Sigma Aldrich, 50 wt%), hydroiodic acid (Sigma Aldrich, 47 wt%, 99.95%), dimethylacetamide (Sigma Aldrich, 99.8%), methylammonium iodide (Great Solar, ≥99.99%), methylammonium chloride (Great Solar, ≥99.99%), formamidinium iodide (Great Solar, ≥99.99%), Cesium iodide (Sigma, 99.9%), lead iodide (TCI, ≥99.5%), lead bromide (TCI, ≥99.5%), lead chloride (TCI, ≥99.5%), tin iodide (TCI, ≥99.5%), Me-4PACz (TCI, ≥99.0%), dimethylformamide (Sigma, 99.8%), dimethylsulfoxide (Sigma, 99.9%), chlorobenzene (Sigma, 99.8%), anisole (Sigma, 99.7%), and toluene (Sigma, 99.8%).

Synthesis of cyclopropylammonium iodide and chloride salts. Cyclopropylammonium iodide and cyclopropylammonium chloride salts were synthesized by dissolving 20 mmol cyclopropylamine in 10 mL ethanol chilled by ice-bath and adding dropwise a 10% stoichiometric excess of HI (57 wt%) or HCl (37 wt%), respectively. The resulting solution was stirred for ten minutes before the excess solvent and acid were removed using a rotary evaporator. The resulting beige powder was washed with ether before being dried over vacuum and stored in a desiccator.

Synthesis of (c-C3A)$_3$(MA)$_3$Pb$_5$I$_{16}$ single crystals by slow cooling in a saturated hydroiodic acid solution. Single crystals of (c-C3A)$_3$(MA)$_3$Pb$_5$I$_{16}$ were synthesized by slow cooling in a saturated hydroiodic acid solution following a procedure already published for hybrid lead halide perovskites.[67, 68] A 1 g scale reaction is prepared by mixing 46.5 mg methylammonium chloride and 307.6 mg PbO in 2.0 mL HI solution (57% w/w) in a 20 mL scintillation vial. To the resulting mixture is added 477.5 μL (50% excess) of a chilled 3 M solution of cyclopropylamine neutralized in H_3PO_2 (45% w/w) solution. The mixture is then heated with magnetic stirring at 120 °C until completely dissolved, after which the stir bar is removed and the hotplate turned off to allow the solution to come to room temperature and crystals to form. The resulting red needle crystals (Figure 1d) are extracted and washed with ether before being dried over vacuum and stored in a desiccator.

Film deposition of $(c\text{-}C3A)_3(MA)_3Pb_5I_{16}$ by spin-coating. Thin films of $(c\text{-}C3A)_3(MA)_3Pb_5I_{16}$ were fabricated by spin-coating 65 μL of a precursor solution of (c-C3A)Cl, (c-C3A)I, (MA)I, and PbI_2 dissolved in dimethylacetamide in a 0.75:3.75:3:5 ratio with 1 M [Pb^{2+}] onto a glass/ITO patterned substrate prepared by UV/Ozone cleaning. The films were spun at 4000 rpm for 30 seconds, and dry nitrogen was blown over the films in the last 10 seconds of spin-coating to encourage nucleation. The resulting thin-films were annealed at 70 °C for 10 min before being stored in a desiccator until characterization. Notably, we found that the width, position, and flow rate of the nitrogen line affected the quality of the films.

Film deposition of 2.0 eV 3D perovskite by spin-coating. Wide-bandgap perovskite precursor solution (1 M, $FA_{0.75}MA_{0.1}Cs_{0.15}PbIBr_2$) was prepared by dissolving CsI, MAI, FAI, and $PbBr_2$ in a mixture of solvents DMF and DMSO at a volume ratio of 4:1. The precursor solution was stirred for 1 h and then filtered using a 0.22 μm polytetrafluoroethylene membrane before use. NiOx nanocrystal (5 mg ml^{-1} in H2O and 2-propanol mixed solvent with a volume ratio of 3:1) layers were first spin-coated on ITO substrates at 3,000 rpm for 25 s in air without any post-treatment, then the substrates were immediately transferred to the glovebox. Me-4PACz (0.4 mg ml^{-1}) in ethanol was spin-coated on the NiO_x film at 3,000 rpm for 30 s and then annealed at 100°C for 10 min. For the perovskite film fabrication, the substrate was spun at 4,000 rpm for 35 s with an acceleration of 1,000 rpm, 100 μL. Anisole was dropped onto the substrate during the last 10 s of spinning. The substrates were then transferred onto a hotplate and heated at 100 °C for 15 min.

$(c\text{-}C3A)_3(MA)_3Pb_5I_{16}$ Solar-cell fabrication. Perovskitoid precursor solution of (c-C3A)Cl, (c-C3A)I, (MA)I, and PbI_2 dissolved in dimethylacetamide in a 0.75:3.75:3:5 ratio with 1 M [Pb^{2+}]. The precursor solution was stirred for 1 h and then filtered using a 0.22 μm polytetrafluoroethylene membrane before use. NiOx nanocrystal (5 mg ml^{-1} in H_2O and 2-propanol mixed solvent with a volume ratio of 3:1) layers were first spin-coated on ITO substrates at 3,000 rpm for 25 s in air without any post-treatment, then the substrates were immediately transferred to the glovebox. Me-4PACz (0.4 mg ml^{-1}) in ethanol was spin-coated on the NiO_x film at 3,000 rpm for 30 s and then annealed at 100°C for 10 min. For perovskite film deposition, 65 μL of precursor solution was added to the stationary film, and the films were spun at 4000 rpm for 30 seconds. Dry nitrogen was blown over the films in the last 10 seconds of spin-coating to encourage nucleation. The resulting thin-films were annealed at 70 °C for 10 min. After cooling down to room temperature,

the substrates were transferred to the evaporation system and 27 nm of C_{60}, 7 nm of BCP and 140 nm of Ag were sequentially deposited on top of the perovskite layer by thermal evaporation.

Single-crystal X-ray diffraction (SCXRD) of $(c\text{-}C3A)_3(MA)_3Pb_5I_{16}$. Intensity data of a red needle single crystal of $(c\text{-}C3A)_3(MA)_3Pb_5I_{16}$ were collected at 250 K. A suitable crystal with dimensions of 0.1×0.067×0.05 mm^3 was mounted on a glass fiber with Paratone oil on a STOE StadiVari diffractometer equipped with an AXO Ag Kα micro-focused sealed X-reay A-MiXS source (λ = 0.560834 Å), running at 65 kV and 0.68 mA, and a Dectris Pilatus3 R CdTe 300K Hybrid photon Counting detector. Data reduction was performed with the X-Area software package using a numerical absorption correction using X-Shape. The structure was solved with the ShelXT structure solution program using the Intrinsic Phasing solution method and Olex2 as the graphical interface. The model was refined with ShelXL using least squares minimization.

Powder and film X-ray diffraction. One-dimensional diffraction patterns were measured on a Rigaku Miniflex600 powder X-ray diffractometer (Cu Kα with graphite monochromator, λ = 1.5406 Å) operating at 40 kV/15 mA with a Kβ foil filter at 10° 2θ/min a 0.02° step-size. Powder diffraction patterns were measured on zero-background Si substrate sample-holders coated, and the powder was fixed to the sample-holder using a thin layer of vacuum grease. Film diffraction patterns were measured directly on the substrate. The height of the substrate produced a rigid shift of ~0.8° 2θ, which has been corrected in the relevant figures. Both film and powder diffraction patterns were measured with the sample rotating.

UV-Vis diffuse reflectance and transmittance spectroscopy. UV-Vis spectra in reflectance mode were collected on ground powder using a Cary 5000 UV-Vis-NIR double beam spectrophotometer with a monochromator. $BaSO_4$ powder was used for the baseline correction, and a mixture of sample powder with $BaSO_4$ was used for the data collection at room temperature. Absorbance data was converted from reflectance data in-software using the Kubelka-Munk equation:

$$\frac{\alpha}{S} = \frac{(1 - R_\infty^2)}{2R_\infty}$$

where α and S are the absorption and scattering coefficients, respectively, and R_∞ is the powder reflectance. UV-Vis transmittance spectra of films were measured directly on the same Cary 5000

UV-Vis-NIR double beam spectrophotometer. A clean substrate was used as a reference for baseline correction.

Photoemission yield spectroscopy in air (PYSA). PYSA measurements were taken on a Riken-Keiki AC-2 spectrometer. Thin film samples were scanned by tunable monochromatic ultraviolet light (UV, 3.8-6.2 eV) under dry air, and emitted photoelectron counts were measured at each excitation energy using an accelerating voltage of 2980 V with a counting time of ten seconds and a step size of 0.1 eV. A detector dead-time of 5.6 ms was used, allowing a maximum counting rate of 1785/s. Maximum signal-to-noise ratio was obtained by setting the UV intensity to 500 nW (1.78 and 2.0 eV 3D perovskite films), 50 nW (1.25 and 1.55 eV 3D perovskite films), and 800 nW ($(c\text{-}C3A)_3(MA)_3Pb_5I_{16}$ crystals), and a quantity-of-light correction was used to account for variations in UV lamp intensity across the energy range. First ionization energies of thin film samples were determined by plotting the third root of photoelectron count rate against excitation energy, and a linear regression was used to determine the onset energy of above-baseline photoelectron flux. The negative of this onset energy was used as an approximation of the energetic position of the valence band maximum of the sample relative to vacuum energy.

Photoluminescence spectroscopy. Photoluminescence on powder and films of $(c\text{-}C3A)_3(MA)_3Pb_5I_{16}$ were performed using an Edinburgh Instruments FS5 spectrofluorimeter using a 150 W xenon arc lamp excitation source and plane-ruled diffraction grating monochromators with 1200 grooves/mm coupled to filter turrets to remove higher order diffraction signals and using a Hamamatsu R928P photomultiplier tube as a primary photodetector and two silicon photodiode detectors for reference and transmission detection. Optical longpass filters were used to control scattered excitation light, with a 340 nm cut-on wavelength for the excitation filter and a 420 nm cut-on wavelength for the emission filter. Confocal PL spectra were collected using a HORIBA LabRAM HR Evolution confocal Raman microscope. A 532 nm laser (0.01% power) was used to excite samples at 10× magnification. Scans were performed in seven windows of 50 nm with 0.2 s acquisition time per window.

Solar cell external quantum efficiency (EQE) measurements. EQE data were acquired using a Quantum Efficiency Measurement System (QE-R) from Enlitech. The light intensity at different wavelengths between 300-1000 nm was calibrated with a factory-calibrated Si cell following ISO 17025 standards.

Solar cell current-voltage (JV) characteristics. The current density - voltage (J-V) curves were obtained using a Keithley 2400 source-measure unit under simulated AM 1.5 G irradiation (100 mW/cm^2) using a Xe arc lamp from a ScienceTech A1 Light Line Class AAA solar simulator. The light from the solar simulator was directed through a fiber optic cable into a nitrogen-atmosphere glovebox (H2O and O2 < 1 ppm). The light intensity, spatial uniformity, and temporal stability were factory-calibrated using traceable reference detectors, and the light intensity was periodically field-checked using a factory-calibrated reference cell, which was itself calibrated on traceable reference equipment.

Computational Methods. First-principles calculations are based on density functional theory (DFT) as implemented in the SIESTA package.[69, 70] The non-local van der Waals density functional of Dion *et al.* corrected by Cooper (C09) is used for geometry optimizations.[71, 72] Spin-orbit coupling is taken into account in subsequent single-point calculations through the off-site approach in the Hemstreet formalism,[73] using the revPBE functional.[74] Core electrons are described with Troullier-Martins pseudopotentials,[75] while valence wavefunctions are developed over double-ζ polarized basis set of finite-range numerical pseudoatomic orbitals.[76] In all cases, an energy cutoff of 150 Ry for real-space mesh size has been used. The Brillouin zones is sampled using a 9×7×3 Γ-centered Monkhorst-Pack grid. Experimental structures are used for the inorganic skeleton, which is well characterized by X-ray diffraction. As this is not the case for light atoms, the positions of organic cations have been optimized.

AUTHOR INFORMATION

Corresponding Authors

*E-mails: ted.sargent@northwestern.edu, m-kanatzidis@northwestern.edu

Notes

The authors declare no competing financial interest.

Author Contributions

This manuscript was written through the contributions of each author. All authors have approved the final version of this manuscript. I.G. prepared and characterized crystal and film samples, performed crystallographic data collection and analysis, and fabricated solar cells. H.W.K., C.L., and Y.Y. assisted in solar cell fabrication and testing. C.H. performed TA measurements. E.O. and R.S. performed VT-Raman spectroscopy measurements, M.K. and J.E. performed DFT calculations. B.V. and S.D.W. performed TEM microscopy and analysis. K.B. fabricated and tested photodetector devices. S.Z. assisted with advanced device measurements. H.W., H.W.K., A.SR.B., and T.E.W. fabricated 3D perovskite films and devices. B.C., E.S., and M.G.K. conceived and supervised the work.

ACKNOWLEDGEMENTS

This work was suported in part the US Department of Energy, Office of Science, Basic Energy Sciences, under award numbers DE-SC0024422 (MGK: synthesis and fundamental studies of metal halides). We also acknowledge support provided by the National Science Foundation under Grant No. DGE-2234667 and CHE-2404059. A.S. R. B. acknowledges support from the King Abdullah University of Science and Technology (KAUST) through the Ibn Rushd Postdoctoral Fellowship award. Work performed at the Center for Nanoscale Materials, a U.S. Department of Energy Office of Science User Facility, was supported by the U.S. DOE, Office of Basic Energy Sciences, under Contract No. DE-AC02-06CH11357.

This work made use of the IMSERC, EPIC, and GIANTFab facilities at Northwestern University. IMSERC has received support from the Soft and Hybrid Nanotechnology Experimental (ShyNE) Resource (NSF ECCS-2025633), the State of Illinois, the International Institute for

Nanotechnology (IIN), and Northwestern University. EPIC has received support from the ShyNE Resource (NSF ECCS-2025633), the IIN, and Northwestern's MRSEC program (NSF DMR-2308961). GIANTFab is supported by the Paula M. Trienens Institute for Sustainability and Energy and the Office of the Vice President for Research at Northwestern.

REFERENCES

(1) Green, M. A.; Dunlop, E. D.; Yoshita, M.; Kopidakis, N.; Bothe, K.; Siefer, G.; Hao, X. Solar cell efficiency tables (version 62). *Progress in Photovoltaics: Research and Applications* **2023**, *31* (7), 651-663.

(2) Bremner, S. P.; Yi, C.; Almansouri, I.; Ho-Baillie, A.; Green, M. A. Optimum band gap combinations to make best use of new photovoltaic materials. *Solar Energy* **2016**, *135*, 750-757.

(3) Zhu, H.; Teale, S.; Lintangpradipto, M. N.; Mahesh, S.; Chen, B.; McGehee, M. D.; Sargent, E. H.; Bakr, O. M. Long-term operating stability in perovskite photovoltaics. *Nature Reviews Materials* **2023**, *8* (9), 569-586.

(4) Grater, L.; Wang, M.; Teale, S.; Mahesh, S.; Maxwell, A.; Liu, Y.; Park, S. M.; Chen, B.; Laquai, F.; Kanatzidis, M. G.; et al. Sterically Suppressed Phase Segregation in 3D Hollow Mixed-Halide Wide Band Gap Perovskites. *The Journal of Physical Chemistry Letters* **2023**, *14* (26), 6157-6162.

(5) Zhao, Y.; Miao, P.; Elia, J.; Hu, H.; Wang, X.; Heumueller, T.; Hou, Y.; Matt, G. J.; Osvet, A.; Chen, Y.-T.; et al. Strain-activated light-induced halide segregation in mixed-halide perovskite solids. *Nature Communications* **2020**, *11* (1), 6328.

(6) Zhang, Z.; Shang, J.; Ge, H.; Zhang, Y.; Chen, Q.; Zhou, L.; Zhu, W.; Chen, D.; Xi, H.; Zhang, J.; et al. Suppressing halide phase segregation in wide-bandgap perovskite film by co-doping strategy for high-performance and stable perovskite solar cells. *Materials Today Physics* **2023**, *37*, 101187.

(7) Liu, H.; Dong, J.; Wang, P.; Shi, B.; Zhao, Y.; Zhang, X. Suppressing the Photoinduced Halide Segregation in Wide-Bandgap Perovskite Solar Cells by Strain Relaxation. *Advanced Functional Materials* **2023**, *33* (41), 2303673.

(8) Rodriguez-Perez, J. J.; Mhamdi, A.; Torres, J.; Montes-Valenzuela, I.; Rivas, J. M.; Esparza, D.; Contreras-Solorio, D. A. Ionic Mobility and Charge Carriers Recombination Analyzed in Triple Cation Perovskite Solar Cells. In *Coatings*, 2023; Vol. 13.

(9) Mao, L.; Stoumpos, C. C.; Kanatzidis, M. G. Two-Dimensional Hybrid Halide Perovskites: Principles and Promises. *Journal of the American Chemical Society* **2019**, *141* (3), 1171-1190.

(10) Leung, T. L.; Ahmad, I.; Syed, A. A.; Ng, A. M. C.; Popović, J.; Djurišić, A. B. Stability of 2D and quasi-2D perovskite materials and devices. *Communications Materials* **2022**, *3* (1), 63.

(11) Kim, E.-B.; Akhtar, M. S.; Shin, H.-S.; Ameen, S.; Nazeeruddin, M. K. A review on two-dimensional (2D) and 2D-3D multidimensional perovskite solar cells: Perovskites structures, stability, and photovoltaic performances. *Journal of Photochemistry and Photobiology C: Photochemistry Reviews* **2021**, *48*, 100405.

(12) Liang, C.; Gu, H.; Xia, Y.; Wang, Z.; Liu, X.; Xia, J.; Zuo, S.; Hu, Y.; Gao, X.; Hui, W.; et al. Two-dimensional Ruddlesden–Popper layered perovskite solar cells based on phase-pure thin films. *Nature Energy* **2021**, *6* (1), 38-45.

(13) Tan, W. L.; Kirby, N. M.; Cheng, Y.-B.; McNeill, C. R. Origin of vertical slab orientation in blade-coated layered hybrid perovskite films revealed with in-situ synchrotron X-ray scattering. *Nano Energy* **2021**, *83*, 105818.

(14) Marjit, K.; Francis, A. G.; Pati, S. K.; Patra, A. Impacts of Exciton Binding Energy and Dielectric Confinement of Layered Lead Halide Perovskites on Carrier Relaxation and Exciton Phonon Interactions. *The Journal of Physical Chemistry Letters* **2023**, *14* (49), 10900-10909.

(15) Zhang, F.; Lu, H.; Larson, B. W.; Xiao, C.; Dunfield, S. P.; Reid, O. G.; Chen, X.; Yang, M.; Berry, J. J.; Beard, M. C.; et al. Surface lattice engineering through three-dimensional lead iodide perovskitoid for high-performance perovskite solar cells. *Chem* **2021**, *7* (3), 774-785.

(16) Cao, S.; Kuang, K.; He, B.; Tang, J.; Yu, Z.; Li, M.; He, Y.; Chen, J. Methylated diammonium spacer modulated three-dimensional lead bromide perovskitoid hybrids with distinct photoconductivity anisotropy. *Inorganic Chemistry Frontiers* **2024**, *11* (14), 4270-4276.

(17) Kour, P.; Chenna Reddy, M.; Pal, S.; Sidhik, S.; Das, T.; Pandey, P.; Mukherjee, S. P.; Chakraborty, S.; Mohite, A. D.; Ogale, S. An Organic–Inorganic Perovskitoid with Zwitterion Cysteamine Linker and its Crystal–Crystal Transformation to Ruddlesden-Popper Phase. *Angewandte Chemie International Edition* **2021**, *60* (34), 18750-18760.

(18) Lin, W.; He, J.; McCall, K. M.; Stoumpos, C. C.; Liu, Z.; Hadar, I.; Das, S.; Wang, H.-H.; Wang, B.-X.; Chung, D. Y.; et al. Inorganic Halide Perovskitoid TlPbI3 for Ionizing Radiation Detection. *Advanced Functional Materials* **2021**, *31* (13), 2006635.

(19) Ma, C.; Gao, L.; Xu, Z.; Li, X.; Song, X.; Liu, Y.; Yang, T.; Li, H.; Du, Y.; Zhao, G.; et al. Centimeter-Sized 2D Perovskitoid Single Crystals for Efficient X-ray Photoresponsivity. *Chemistry of Materials* **2022**, *34* (4), 1699-1709.

(20) Stoumpos, C. C.; Mao, L.; Malliakas, C. D.; Kanatzidis, M. G. Structure–Band Gap Relationships in Hexagonal Polytypes and Low-Dimensional Structures of Hybrid Tin Iodide Perovskites. *Inorganic Chemistry* **2017**, *56* (1), 56-73.

(21) Umeyama, D.; Leppert, L.; Connor, B. A.; Manumpil, M. A.; Neaton, J. B.; Karunadasa, H. I. Expanded Analogs of Three-Dimensional Lead-Halide Hybrid Perovskites. *Angewandte Chemie International Edition* **2020**, *59* (43), 19087-19094.

(22) Fan, C.-C.; Liang, B.-D.; Liu, C.-D.; Chai, C.-Y.; Han, X.-B.; Zhang, W. Stable organic lead iodides with three-dimensional crystallographic and electronic structures showing high photoresponse. *Inorganic Chemistry Frontiers* **2022**, *9* (24), 6404-6411.

(23) Li, X.; He, Y.; Kepenekian, M. l.; Guo, P.; Ke, W.; Even, J.; Katan, C.; Stoumpos, C. C.; Schaller, R. D.; Kanatzidis, M. G. Three-Dimensional Lead Iodide Perovskitoid Hybrids with High X-ray Photoresponse. *Journal of the American Chemical Society* **2020**, *142* (14), 6625-6637.

(24) Wilke, M.; Casati, N. Insight into the Mechanochemical Synthesis and Structural Evolution of Hybrid Organic–Inorganic Guanidinium Lead(II) Iodides. *Chemistry – A European Journal* **2018**, *24* (67), 17701-17711.

(25) Ben Haj Salah, M.; Tessier, J.; Mercier, N.; Allain, M.; Leblanc, A.; Che, X.; Katan, C.; Kepenekian, M. A 3D Lead Iodide Hybrid Based on a 2D Perovskite Subnetwork. *Crystals* **2021**, *11* (12), 1570.

(26) Louvain, N.; Mercier, N. A 3D metal halide framework in the organic–inorganic compound (H3N(CH2)2SS(CH2)2NH3)3Pb5I16. *Solid State Sciences* **2008**, *10* (10), 1269-1275.

(27) Zhang, F.; Park, S. Y.; Yao, C.; Lu, H.; Dunfield, S. P.; Xiao, C.; Uličná, S. a.; Zhao, X.; Du Hill, L.; Chen, X.; et al. Metastable Dion-Jacobson 2D structure enables efficient and stable perovskite solar cells. *Science* **2022**, *375* (6576), 71-76.

(28) Keerthisinghe, N.; Christian, M. S.; Berseneva, A. A.; Morrison, G.; Klepov, V. V.; Smith, M. D.; zur Loye, H.-C. Investigation of Metastable Low Dimensional Halometallates. *Molecules* **2022**, *27* (1), 280.

(29) Ge, B.-D.; Wei, Q.; Sun, A.-H.; Lin, C.-Y.; Duan, X.-F.; Li, J.-H.; Wang, G.-M. A 3D Iodoplumbate Semiconducting Open Framework with Visible-light-induced Photocatalytic Performance. *Chemistry – An Asian Journal* **2019**, *14* (12), 2086-2090.

(30) Xie, G.; Wang, L.; Ju, D.; Yao, C.; Wang, X.; Song, S.; Qu, Y.; Li, H.; Tao, X. Thermochromism Perovskite (COOH(CH2)3NH3)2PbI4 Crystals: Single-Crystal to Single-Crystal Phase Transition and Excitation-Wavelength-Dependent Emission. *The Journal of Physical Chemistry Letters* **2022**, *13* (1), 214-221.

(31) Yang, X.; Wang, X.-D.; Li, W.-G.; Huang, Y.-H.; Wang, L.-B.; Liu, J.-M.; Jiang, L.; Kuang, D.-B. Conjugated diamine cation based halide perovskitoid enables robust stability and high photodetector performance. *Science Bulletin* **2024**.

(32) Liu, C.; Yang, Y.; Chen, H.; Spanopoulos, I.; Bati, A. S. R.; Gilley, I. W.; Chen, J.; Maxwell, A.; Vishal, B.; Reynolds, R. P.; et al. Two-dimensional perovskitoids enhance stability in perovskite solar cells. *Nature* **2024**, *633* (8029), 359-364.

(33) Nan, Z.-A.; Chen, L.; Liu, Q.; Wang, S.-H.; Chen, Z.-X.; Kang, S.-Y.; Ji, J.-B.; Tan, Y.-Y.; Hui, Y.; Yan, J.-W.; et al. Revealing phase evolution mechanism for stabilizing formamidinium-based lead halide perovskites by a key intermediate phase. *Chem* **2021**, *7* (9), 2513-2526.

(34) Ji, C.; Zhu, T.; Fan, Y.; Li, Z.; Liu, X.; Li, L.; Sun, Z.; Luo, J. Localized Lattice Expansion of $FAPbBr_3$ to Design a 3D Hybrid Perovskite for Sensitive Near‐Infrared Photodetection. *Angewandte Chemie International Edition* **2022**, *61* (47).

(35) Li, R.; Jiang, H.; Yao, Y.; Ye, H.; Liu, X.; Chen, S.; Luo, J. Bulk Single Crystals of a Narrow Band Gap Three-Dimensional Hybrid Perovskitoid Enabling Ultrastable Photodetection. *Chemistry of Materials* **2022**, *34* (23), 10382-10389.

(36) Sun, C.; Wang, M. S.; Li, P. X.; Guo, G. C. Conductance Switch of a Bromoplumbate Bistable Semiconductor by Electron‐Transfer Thermochromism. *Angewandte Chemie International Edition* **2016**, *56* (2), 554-558.

(37) Zhang, H.-Y.; Song, X.-J.; Cheng, H.; Zeng, Y.-L.; Zhang, Y.; Li, P.-F.; Liao, W.-Q.; Xiong, R.-G. A Three-Dimensional Lead Halide Perovskite-Related Ferroelectric. *Journal of the American Chemical Society* **2020**, *142* (10), 4604-4608.

(38) Liu, G.; Liu, J.; Tao, X.; Li, D.-s.; Zhang, Q. Surfactants as additives make the structures of organic–inorganic hybrid bromoplumbates diverse. *Inorganic Chemistry Frontiers* **2016**, *3* (11), 1388-1392.

(39) Tang, Y.-Y.; Liu, Y.-H.; Peng, H.; Deng, B.-B.; Cheng, T.-T.; Hu, Y.-T. Three-Dimensional Lead Bromide Hybrid Ferroelectric Realized by Lattice Expansion. *Journal of the American Chemical Society* **2020**, *142* (46), 19698-19704.

(40) Tian, J.; Cordes, D. B.; Slawin, A. M. Z.; Zysman-Colman, E.; Morrison, F. D. Progressive Polytypism and Bandgap Tuning in Azetidinium Lead Halide Perovskites. *Inorganic Chemistry* **2021**, *60* (16), 12247-12254.

(41) Elliott, C.; McNulty, J. A.; Cordes, D. B.; Slawin, A. M. Z.; Lightfoot, P. Structural diversity in hybrid lead halides templated by 4-methylimidazolium. *Journal of Solid State Chemistry* **2021**, *303*, 122466.

(42) Smółka, S.; Mączka, M.; Drozdowski, D.; Stefańska, D.; Gągor, A.; Sieradzki, A.; Zaręba, J. K.; Ptak, M. Effect of Dimensionality on Photoluminescence and Dielectric Properties of Imidazolium Lead Bromides. *Inorganic Chemistry* **2022**, *61* (38), 15225-15238.

(43) Geselle, M.; Fuess, H. Crystal structure of dimethylammonium tribromoplumbate(II), (CH3)2NH2PbBr3. *Zeitschrift für Kristallographie - New Crystal Structures* **1997**, *212* (1), 234-234.

(44) Kaltzoglou, A.; Elsenety, M. M.; Koutselas, I.; Kontos, A. G.; Papadopoulos, K.; Psycharis, V.; Raptopoulou, C. P.; Perganti, D.; Stergiopoulos, T.; Falaras, P. Synthesis, characterization and optoelectronic properties of chemically stable (CH 3) 3 SPbI 3− x Br x and (CH 3) 3 SPbI 3− x Cl x (x = 0, 1, 2, 3) perovskites. *Polyhedron* **2018**, *140*, 67-73.

(45) García-Espejo, G.; Konidaris, K. F.; Guagliardi, A.; Masciocchi, N. Using Imidazolium in the Construction of Hybrid 2D and 3D Lead Bromide Pseudoperovskites. *Chemistry* **2023**, *5* (2), 1329-1343.

(46) García-Fernández, A.; Juarez-Perez, E. J.; Bermúdez-García, J. M.; Llamas-Saiz, A. L.; Artiaga, R. n.; López-Beceiro, J. J.; Señarís-Rodríguez, M. a. A.; Sánchez-Andújar, M.; Castro-García, S. Hybrid lead halide [(CH3)2NH2]PbX3(X = Cl−and Br−) hexagonal perovskites with multiple functional properties. *Journal of Materials Chemistry C* **2019**, *7* (32), 10008-10018.

(47) Li, X.; Do, T. T. H.; Granados del Águila, A.; Huang, Y.; Chen, W.; Xiong, Q.; Zhang, Q. A 3D Haloplumbate Framework Constructed From Unprecedented Lindqvist‐like Highly

Coordinated $[Pb_6Br_{25}]^{13-}$ Nanoclusters with Temperature‐Dependent Emission. *Chemistry – An Asian Journal* **2018**, *13* (21), 3185-3189.

(48) Song, K.; Du, L.; Yue, G.; Li, T.; Li, H.; Zheng, S.; Chen, Z.; Zheng, H. Simultaneously elevating the resistive switching level and ambient-air-stability of 3D perovskite (TAZ-H)PbBr3-based memory device by encapsulating into polyvinylpyrrolidone. *Journal of Colloid and Interface Science* **2023**, *642*, 408-420.

(49) Jung, M.-H. The dual band and white-light emission from piperazine halide perovskites. *CrystEngComm* **2022**, *24* (7), 1413-1423.

(50) Mao, L.; Guo, P.; Kepenekian, M. l.; Hadar, I.; Katan, C.; Even, J.; Schaller, R. D.; Stoumpos, C. C.; Kanatzidis, M. G. Structural Diversity in White-Light-Emitting Hybrid Lead Bromide Perovskites. *Journal of the American Chemical Society* **2018**, *140* (40), 13078-13088.

(51) Lassoued, M. S.; Luo, Q.-C.; Zheng, Y.-Z. A 3D lead chloride hybrid exhibits self-trapped emission and exceptional stability. *Inorganic Chemistry Frontiers* **2023**, *10* (21), 6392-6400.

(52) Wang, G.-E.; Xu, G.; Wang, M.-S.; Cai, L.-Z.; Li, W.-H.; Guo, G.-C. Semiconductive 3-D haloplumbate framework hybrids with high color rendering index white-light emission. *Chemical Science* **2015**, *6* (12), 7222-7226.

(53) Peng, Y.; Li, L.; Ji, C.; Wu, Z.; Wang, S.; Liu, X.; Yao, Y.; Luo, J. Tailored Synthesis of an Unprecedented Pb–Mn Heterometallic Halide Hybrid with Enhanced Emission. *Journal of the American Chemical Society* **2019**, *141* (31), 12197-12201.

(54) Jung, M.-H.; Ko, K. C.; Lee, W. R. Broadband white-light emission from supramolecular piperazinium-based lead halide perovskites linked by hydrogen bonds. *Dalton Transactions* **2019**, *48* (40), 15074-15090.

(55) Li, X.; Kepenekian, M. l.; Li, L.; Dong, H.; Stoumpos, C. C.; Seshadri, R.; Katan, C.; Guo, P.; Even, J.; Kanatzidis, M. G. Tolerance Factor for Stabilizing 3D Hybrid Halide Perovskitoids Using Linear Diammonium Cations. *Journal of the American Chemical Society* **2022**, *144* (9), 3902-3912.

(56) Billing, D. G.; Lemmerer, A. Inorganic–organic hybrid materials incorporating primary cyclic ammonium cations: The lead iodide series. *CrystEngComm* **2007**, *9* (3), 236-244.

(57) Hoffman, J. M.; Che, X.; Sidhik, S.; Li, X.; Hadar, I.; Blancon, J.-C.; Yamaguchi, H.; Kepenekian, M. l.; Katan, C.; Even, J.; et al. From 2D to 1D Electronic Dimensionality in Halide Perovskites with Stepped and Flat Layers Using Propylammonium as a Spacer. *Journal of the American Chemical Society* **2019**, *141* (27), 10661-10676.

(58) Vasileiadou, E. S.; Jiang, X.; Kepenekian, M. l.; Even, J.; De Siena, M. C.; Klepov, V. V.; Friedrich, D.; Spanopoulos, I.; Tu, Q.; Tajuddin, I. S.; et al. Thick-Layer Lead Iodide Perovskites with Bifunctional Organic Spacers Allylammonium and Iodopropylammonium Exhibiting Trap-State Emission. *Journal of the American Chemical Society* **2022**, *144* (14), 6390-6409.

(59) Jung, M.-H. Exploration of two-dimensional perovskites incorporating methylammonium for high performance solar cells. *CrystEngComm* **2021**, *23* (5), 1181-1200.

(60) Billing, D. G.; Lemmerer, A. Octakis(3-propylammonium) octadecaiodopentaplumbate(II): a new layered stucture based on layered perovskites. *Acta Crystallographica Section C* **2006**, *62* (6), m238-m240.

(61) Yaffe, O.; Guo, Y.; Tan, L. Z.; Egger, D. A.; Hull, T.; Stoumpos, C. C.; Zheng, F.; Heinz, T. F.; Kronik, L.; Kanatzidis, M. G.; et al. Local Polar Fluctuations in Lead Halide Perovskite Crystals. *Physical Review Letters* **2017**, *118* (13), 136001.

(62) Lanigan-Atkins, T.; He, X.; Krogstad, M. J.; Pajerowski, D. M.; Abernathy, D. L.; Xu, G. N. M. N.; Xu, Z.; Chung, D. Y.; Kanatzidis, M. G.; Rosenkranz, S.; et al. Two-dimensional overdamped fluctuations of the soft perovskite lattice in CsPbBr3. *Nature Materials* **2021**, *20* (7), 977-983.

(63) Endres, J.; Egger, D. A.; Kulbak, M.; Kerner, R. A.; Zhao, L.; Silver, S. H.; Hodes, G.; Rand, B. P.; Cahen, D.; Kronik, L.; et al. Valence and Conduction Band Densities of States of Metal Halide Perovskites: A Combined Experimental–Theoretical Study. *The Journal of Physical Chemistry Letters* **2016**, *7* (14), 2722-2729.

(64) Liu, Y.; Banon, J.-P.; Frohna, K.; Chiang, Y.-H.; Tumen-Ulzii, G.; Stranks, S. D.; Filoche, M.; Friend, R. H. The Electronic Disorder Landscape of Mixed Halide Perovskites. *ACS Energy Letters* **2023**, *8* (1), 250-258.

(65) Wuttig, M.; Schön, C.-F.; Schumacher, M.; Robertson, J.; Golub, P.; Bousquet, E.; Gatti, C.; Raty, J.-Y. Halide Perovskites: Advanced Photovoltaic Materials Empowered by a Unique Bonding Mechanism. *Advanced Functional Materials* **2022**, *32* (2), 2110166.

(66) Wang, J.; Zeng, L.; Zhang, D.; Maxwell, A.; Chen, H.; Datta, K.; Caiazzo, A.; Remmerswaal, W. H. M.; Schipper, N. R. M.; Chen, Z.; et al. Halide homogenization for low energy loss in 2-eV-bandgap perovskites and increased efficiency in all-perovskite triple-junction solar cells. *Nature Energy* **2024**, *9* (1), 70-80.

(67) Stoumpos, C. C.; Cao, D. H.; Clark, D. J.; Young, J.; Rondinelli, J. M.; Jang, J. I.; Hupp, J. T.; Kanatzidis, M. G. Ruddlesden–Popper Hybrid Lead Iodide Perovskite 2D Homologous Semiconductors. *Chemistry of Materials* **2016**, *28* (8), 2852-2867.

(68) Mao, L.; Ke, W.; Pedesseau, L.; Wu, Y.; Katan, C.; Even, J.; Wasielewski, M. R.; Stoumpos, C. C.; Kanatzidis, M. G. Hybrid Dion–Jacobson 2D Lead Iodide Perovskites. *Journal of the American Chemical Society* **2018**, *140* (10), 3775-3783.

(69) José, M. S.; Emilio, A.; Julian, D. G.; Alberto, G.; Javier, J.; Pablo, O.; Daniel, S.-P. The SIESTA method for ab initio order-N materials simulation. *Journal of Physics: Condensed Matter* **2002**, *14* (11), 2745.

(70) García, A.; Papior, N.; Akhtar, A.; Artacho, E.; Blum, V.; Bosoni, E.; Brandimarte, P.; Brandbyge, M.; Cerdá, J. I.; Corsetti, F.; et al. Siesta: Recent developments and applications. *The Journal of Chemical Physics* **2020**, *152* (20), 204108.

(71) Dion, M.; Rydberg, H.; Schröder, E.; Langreth, D. C.; Lundqvist, B. I. Van der Waals Density Functional for General Geometries. *Physical Review Letters* **2004**, *92* (24), 246401.

(72) Cooper, V. R. Van der Waals density functional: An appropriate exchange functional. *Physical Review B* **2010**, *81* (16), 161104.

(73) Cuadrado, R.; Cerdá, J. I. Fully relativistic pseudopotential formalism under an atomic orbital basis: spin–orbit splittings and magnetic anisotropies. *Journal of Physics: Condensed Matter* **2012**, *24*, 086005.

(74) Zhang, Y.; Yang, W. Comment on ``Generalized Gradient Approximation Made Simple". *Physical Review Letters* **1998**, *80* (4), 890-890.

(75) Troullier, N.; Martins, J. L. Efficient pseudopotentials for plane-wave calculations. *Physical Review B* **1991**, *43* (3), 1993-2006.

(76) Artacho, E.; Sánchez-Portal, D.; Ordejón, P.; García, A.; Soler, J. M. Linear-Scaling ab-initio Calculations for Large and Complex Systems. *physica status solidi (b)* **1999**, *215* (1), 809-817.

TOC Graphic

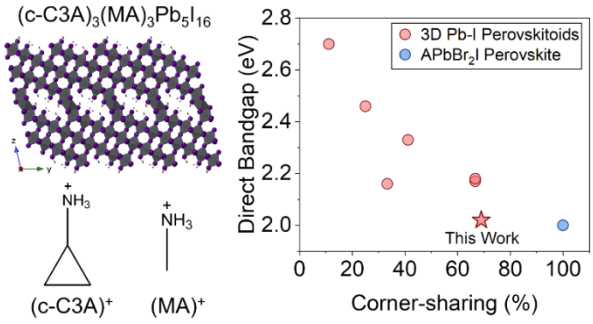
(c-C3A)3(MA)3Pb5I16
NH3
NH3
(c-C3A)+
(MA)+
3D Pb-I Perovskitoids
APbBr2I Perovskite
This Work
Direct Bandgap (eV)
Corner-sharing (%)
2.8
2.6
2.4
2.2
2.0
0
20
40
60
80
100